



Regional PM_{2.5} pollution confined by atmospheric internal boundaries in the North China Plain: 2. boundary layer structures and numerical simulation

Xipeng Jin¹, Xuhui Cai^{1*}, Mingyuan Yu², Yu Song¹, Xuesong Wang¹, Hongsheng Zhang³, Tong Zhu¹

¹College of Environmental Sciences and Engineering, State Key Lab of Environmental Simulation and Pollution Control, Peking University, Beijing 100871, China

²School of Applied Meteorology, Nanjing University of Information Science and Technology, Nanjing 210044, China

³Department of Atmospheric and Oceanic Sciences, School of Physics, Peking University, Beijing 100871, China

Correspondence to: Xuhui Cai (E-mail: xhcai@pku.edu.cn)

1 **Abstract.** This study reveals and summarizes mesoscale planetary boundary layer (PBL) structures for
2 various pollution patterns in the North China Plain. Three pollution categories have been classified, in
3 terms of the influence of the atmospheric internal boundary (AIB) that significantly determines the
4 distribution and concentration of PM_{2.5}. The Weather Research and Forecast model is used to simulate
5 the PBL structure in this region, and its performance is firstly evaluated using surface observations and
6 intensive soundings data. Observed AIBs and PBL evolution are reasonably reproduced. Simulation
7 results for three pollution categories illustrate respective PBL structures, as well the relationship with the
8 mesoscale AIBs. The first category corresponds to the severest pollution and occurs most frequently
9 (~41 %). The PBL structure is laterally confined by a warm front as a sharp AIB and vertically suppressed
10 by a dome-like elevated temperature inversion, which constitutes a stable and enclosed circumstance,
11 most favorable to pollution formation. The second category is characterized by wind shear line/zone as
12 AIB, with dynamic convergence in the PBL as the dominant cause for PM_{2.5} accumulation. Three shear
13 modes consist of this category, two of which are related to pressure troughs with the convergence layer
14 of the order of the PBL depth. Another shear mode presents a much thicker convergence layer with a
15 depth of about 3000 m, under the saddle-shaped pressure field. This category corresponds to lighter air
16 pollution, with a frequency of 29 %. The PBL of the third category is laterally delineated by a cold-air
17 damming AIB at the foot of the mountains on the windward side. It manifests as a low-temperature and
18 weak-wind air mass accompanied by an elevated inversion and a convergent flow with a thickness as
19 high as mountains. This PBL structure maintains through day and night within the AIB confined zone,
20 while the ordinary diurnal variation of the PBL occurs outside this zone. 14 % of pollution episodes



21 belong to this category. There remain about 16 % pollution episodes undefined by the AIB influence.
22 They may need to be analyzed separately in the future.

23 **Keywords:** Boundary layer structure; atmospheric internal boundaries; PM_{2.5}; modeling

24 **1 Introduction**

25 The planetary boundary layer (PBL) is the lowest section of the atmosphere that responds directly
26 to the heat and friction from the Earth's surface (Stull, 1988; Garratt, 1992). Most air pollutants are
27 intensively emitted or chemically produced within this layer, and their horizontal transport and vertical
28 mixing are affected by the dynamic flow and thermal stability of the PBL (Tennekes, 1974). Therefore,
29 the PBL structure is a crucial role in the evolution, magnitude and distribution of air pollution.

30 The PBL structure has been recognized to be strongly dependent on three categories of factors: (i)
31 the single-column vertical property forced by the local surface's energy balance; (ii) the lateral-section
32 horizontal variation regulated by the mesoscale meteorological process and (iii) the three-dimensional
33 spatial evolution controlled by the large-scale synoptic system (Boutle et al., 2010). The local vertical
34 PBL structure and its impact on air pollution have been widely discussed from different aspects including
35 turbulent mixing (Emeis and Schafer, 2006; Ren et al., 2019), dynamic effect (Dupont et al., 2016),
36 entrainment (Li et al., 2018; Jin et al., 2020), and radiative feedback with aerosol (Petaja, 2016). In these
37 studies, the PBL height at a certain site has been the most commonly used indicator to analyze the
38 correlation with pollutant concentration, whether from the time scale of the diurnal cycle, daily variation,
39 or longer period (Bianco et al., 2011; Liu et al., 2019; Miao and Liu, 2019). Moreover, some studies
40 investigate the PBL spatial structure under the large-scale force of weather systems (Prezerakos, 1998;
41 Boutle et al., 2010; Mayfield and Fochesatto, 2013). Sinclair et al. (2010) report the three-dimensional
42 PBL structure developed beneath an idealized mid-latitude weather system, which is characterized by a
43 deep convective PBL in the eastern flanks of the anticyclone and a shallow shear-driven PBL in the
44 cyclone's warm sector. The effect of the monsoon trough on the PBL has also been indicated, showing
45 relatively low PBL capped by a stable layer in the western end of the trough line, while a well-defined
46 deep moist layer with active thermal instability in the eastern end (Rajkumar et al., 1994; Narasimha,
47 1997; Potty et al., 2001). In recent years, synoptic classification has been used to explore the role of
48 different weather circulations on PBL structure and to further analyze air pollution (Peng et al., 2016;
49 Xiao et al., 2020). The movement of the synoptic systems makes the shallow and deep boundary layers
50 develop alternately in a certain area, regulating the periodic evolution of large-scale air pollution.

51 As the intermediate, mesoscale systems interact with PBL in more direct and complex ways, since
52 they occur in the low-level troposphere with vertical extension comparable with the PBL depth and
53 horizontal scale closing to the regional range. Discontinuity of meteorological properties inside and



54 outside these systems presents as atmospheric internal boundary (AIB) in the lateral direction, leading to
55 the abrupt change of the PBL spatial structure, which is of particular importance to the formation and
56 maintenance of regional pollution. The effects of mesoscale sea-land and mountain-valley circulations
57 on the PBL have been clarified, i.e., the thermal internal boundary layer in the coastal area and the
58 depressed PBL close to a mountain base (Garratt, 1990; Lu and Turco, 1995; Talbot et al., 2007; De
59 wekker, 2008; Miao et al., 2015). Some studies discuss the PBL structure under the rule of other types
60 of mesoscale/sub-synoptic scale systems, such as the persistent cold-air pools in the Salt Lake valley
61 (Lareau et al., 2013), foehn winds in the Eastern Alps (Seibert, 1990; Baumann et al., 2001), and leeside
62 troughs and cold-air damming around the Appalachian mountains (Seaman and Michelson, 2000; Bell
63 and Bosart, 1988), as well as the frequent cold and warm fronts in Europe (Berger and Friehe, 1995;
64 Sinclair, 2013). However, there needs more understanding of their impact on the evolution of air pollution.

65 The North China Plain (NCP) is one of the most polluted areas in the world, to which extensive
66 investigation has been conducted. Nevertheless, the knowledge about the PBL spatial structures under
67 the impact of the mesoscale systems and the role AIBs play in this region is still insufficient. Based on
68 the surface observations, a thorough survey of the PM_{2.5} pollution categories under the control of the
69 AIBs is carried out in a companion paper (Jin et al., 2022 submitted). It is found that the pollution
70 formation-maintenance process in the NCP can be classified into three categories, i.e., the frontal
71 category, wind shear category and topographic obstruction category respectively. The first category
72 represents about 41 % of all episodes during the autumn and winter of the investigated 7 years (2014–
73 2020). An isolated cold area is bounded by a warm front, which plays as the AIB. The second category
74 is determined by dynamic wind shears. Three modes of AIBs are characterized by west-southwest wind
75 shear, southeast-east wind shear and south-north wind shear respectively. The third category is closely
76 related to the cold-air damming effect with the AIB formed between the prevailing airflow and the
77 blocked air toward the terrain. Although the results in Jin et al. (2022 submitted) clearly demonstrate the
78 relationship of the surface AIBs to the pollution episodes and their spatial patterns, the three-dimensional
79 structures of these mesoscale AIBs and their interplay with the PBL are not yet clarified, those are
80 believed to be of critical significance to the regional pollution. The present study tries to fulfill this
81 knowledge gap.

82 The mesoscale meteorological models, such as the Weather Research and Forecast (WRF) with the
83 high spatial and temporal resolution, are plausible tools to capture the mesoscale systems and display
84 detailed spatial structures in the lower atmosphere, including the AIBs and the PBL (Jimenez et al., 2016,
85 Pielke and Uliasz, 1998; Seaman, 2000; Hanna and Yang, 2001; McNider and Pour-Biazar, 2020). The
86 present study aims to reveal the thermal and dynamic structures of the PBL and their evolution associate
87 with different types of AIBs in the condition of pollution episodes, by using the WRF model simulations.
88 For this purpose, the model performance is at first evaluated with detailed sounding data from the



89 intensive experiment, to ensure the model's ability in reproducing the meteorological fields and their
90 three-dimension structures in the concerned region. The article is organized as follows. The following
91 section describes the PBL sounding observations as well as the WRF simulation. Section 3 provides an
92 overview of representative pollution cases and the evaluation of the model performance. Furthermore,
93 the PBL spatial structure under each pollution category is analyzed. Finally, the conclusions are presented
94 and the feasibility and limitation of mesoscale models are discussed in Sect. 4.

95 **2 Data and methods**

96 **2.1 Observations and data analysis**

97 **Intensive GPS (Global Positioning System) sounding data:** Two periods of field experiments
98 were carried out to evaluate the meteorological model and explore wintertime PBL structure in the NCP:
99 at Cangzhou (38°13' N, 117°48' E, Fig. 1a) from January 8 to 28, 2016 and at Dezhou (37°16' N, 116°43'
100 E, Fig. 1a) from December 25, 2017, to January 24. GPS radiosonde (Beijing Changzhi Sci & Tech Co.
101 Ltd., China) was used to obtain profiles of wind speed, wind direction, temperature and relative humidity
102 with a vertical resolution of approximately 1 s (3~5 m). Eight soundings were taken on each day, at 0200,
103 0500, 0800, 1100, 1400, 1700, 2000 and 2300 LT (i.e., UTC + 8). The reliability of the GPS sounding
104 data has been systematically evaluated by Li et al. (2020) and Jin et al. (2020, 2021).

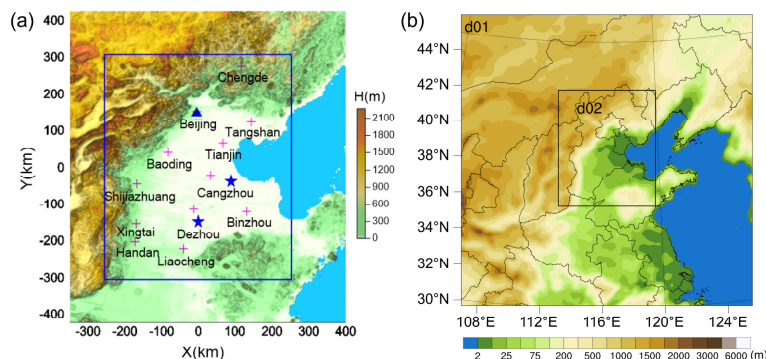
105 **Routine radiosonde sounding data:** Routine sounding data from the meteorological station of
106 Beijing (39°56' N, 116°17' E, Fig. 1a) was collected in the absence of intensive PBL observation. The
107 data were obtained from Wyoming University, USA (<http://weather.uwyo.edu.html>), and the original
108 observation data came from the China Meteorological Administration. The routine soundings were taken
109 2 times a day, at 0800 and 2000 LT.

110 **PBL height and vertical profiles:** During the two periods of intensive field experiments, 160 and
111 240 datasets were collected at each site, including vertical profiles of temperature, relative humidity,
112 wind speed, and wind direction. We carried out quality control on the original sounding data and
113 eliminated outliers and then calculated the profiles of potential temperature. All the profiles were
114 smoothed by the three-point moving average method and were interpolated to obtain a vertical resolution
115 of 10 m. The PBL height was derived via the potential temperature profile method and the detailed
116 calculation followed the mathematical method established by Liu and Liang (2010). Sounding data were
117 used to evaluate model performance and to analyze the three-dimensional thermal and dynamic spatial
118 structure of the PBL.

119 In addition to the PBL sounding data, the routine meteorological observation and air quality
120 monitoring data were used to obtain the surface meteorological field and pollutant concentration field.
121 The spatial distributions of sea level pressure, 10 m wind vector, potential temperature and the



122 corresponding $PM_{2.5}$ concentration were obtained by data interpolation or diagnostic model, details of
123 the methods referred to Jin et al. (2021).



124
125 Figure 1. Geographical map of the (a) observation area and (b) WRF model domain. Intensive GPS
126 soundings at Dezhou and Cangzhou (pentagram), routine radiosonde sounding at Beijing (triangle) and
127 air quality stations (plus) are indicated in (a). The rectangle in (a) is the same as the model inner domain
128 d02 in (b).

129 2.2 Model simulations

130 The WRF model was used to investigate the vertical and horizontal structures of the PBL. Two
131 nested domains (Fig. 1b) were employed with horizontal grid resolutions of 15 and 5 km. Each domain
132 had 37 vertical layers extending from the surface to 100 hPa, with 25 layers within 2 km to resolve the
133 PBL structure. The meteorological initial and boundary conditions were set using the United States
134 National Center for Environmental Prediction Final Analysis (NCEP-FNL) dataset. The physics
135 parameterization schemes applied in this study were the same as Jin et al. (2021).

136 2.3 Representative cases

137 As mentioned above, three categories, six types of $PM_{2.5}$ pollution episodes associated with
138 mesoscale AIBs have been identified in the NCP (Jin et al. 2022 submitted). The present study tries to
139 reveal the PBL structures and their evolution for these pollution and AIB types. Typical cases
140 representative of the respective types were selected for this purpose. For the first category, two frontal
141 types shared a similar PBL structure and have been investigated previously (Jin et al., 2021), which would
142 be recapitulated in the following section. In the second category, the southeast-east wind shear type had
143 a very low occurrence frequency (4 %) and showed similar characteristics to the west-southwest wind
144 shear type. Therefore, the two main types of wind shear category and topographic obstruction category
145 were investigated in this paper. Three typical cases/episodes were selected to respectively represent the
146 corresponding pollution types, i.e., Case-1 for west-southwest wind shear type: during January 18–21,



147 2018; Case-2 for south-north wind shear type: during January 7–11, 2016; and Case-3 for topographic
148 obstruction type: during October 7–12, 2014. The temporal and spatial evolution of their PM_{2.5}
149 concentrations and the corresponding surface meteorological conditions would be analyzed based on
150 routine observations, and their PBL spatial structures would be revealed by the WRF model simulations.

151 3 Results

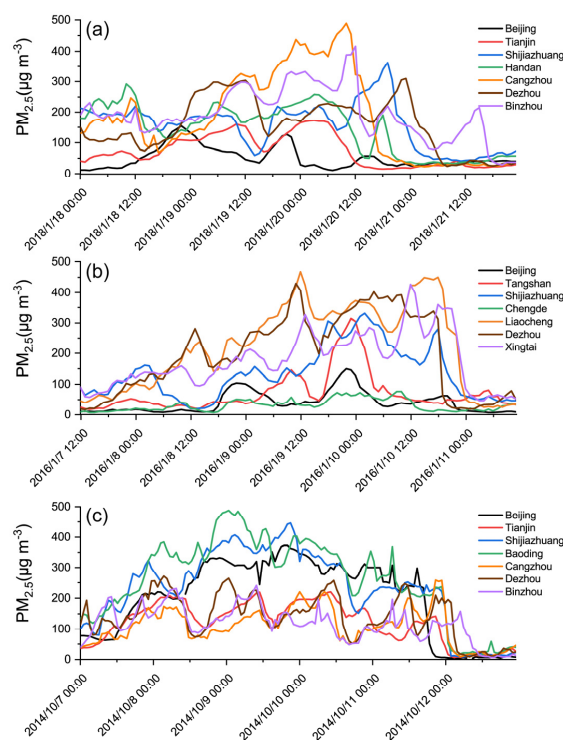
152 3.1 Basic features of the cases

153 The surface observations for these three cases are presented firstly. According to the temporal
154 evolution of PM_{2.5} concentration at different stations in the NCP (Fig. 2), all of these three pollution
155 episodes went through the stages of formation, maintenance and diffusion. As shown in Fig. 2a, Case-1
156 was characterized by two main peaks in the formation-maintenance stage (January 18–20, 2018), with
157 the latter being higher than the former (500 $\mu\text{g m}^{-3}$ at Canzhou vs 300 $\mu\text{g m}^{-3}$ at Handan). From noon on
158 January 20, 2018, pollution in Tianjin-Cangzhou-Shijiazhuang diffused successively and all sites reached
159 a clean level on the afternoon of January 21, 2018. For Case-2, the pollution formed in the first two days,
160 maintained over the next day and was cleaned on the night of January 10, 2016 (Fig. 2b). The southern
161 sites such as Liaocheng and Dezhou were the most polluted (reaching 450 $\mu\text{g m}^{-3}$) and the northern cities
162 such as Beijing and Chengde were the least polluted (less than 150 $\mu\text{g m}^{-3}$). Pollution in Case-3
163 experienced the formation process on October 7–8, 2014, maintained for the successive three days, and
164 ended on October 12, 2014 (Fig. 2c). During this period, the piedmont sites (Baoding, Beijing and
165 Shijiazhuang) kept always a high concentration regardless of day and night (about 400 $\mu\text{g m}^{-3}$), while
166 the southeast sites (Binzhou, Dezhou and Cangzhou) had lighter pollution and obvious diurnal cycle
167 (lower than 250 $\mu\text{g m}^{-3}$).

168 The spatial patterns of PM_{2.5} pollution, from the formation (Fig. 3i), maintenance (Fig. 3ii-iv), to
169 diffusion stage (Fig. 3v), are illustrated for each case. In the formation stage, the polluted air mass of
170 Case-1 and Case-3 built up along the mountains from the southwest of the NCP (Fig. 3a-i, c-i) while it
171 was located more south in Case-2 (Fig. 3b-i). During the pollution maintenance process, Case-1 was
172 accompanied by widespread PM_{2.5} flooding the NCP, during which the heaviest pollution center has been
173 transferred eastward (Fig. 3a, ii-iv); in Case-2, a polluted air mass has been advancing northward with a
174 clear edge, but it did not reach the northern mountainous area (Fig. 3b, ii-iv); the spatial distribution of
175 PM_{2.5} of Case-3 was characterized by the day-night contrast, manifested as pollution filling the entire
176 plain area at night while concentrating in front of the mountains with a distinct edge on the southeast side
177 during the daytime (Fig. 3c, ii-iv). Finally, these pollution cases were diffused in different ways. In Case-
178 1, the clean air first occupied the northern parts of the NCP with a large concentration gradient on the
179 front edges (Fig. 3a, v). As for Case-2, PM_{2.5} was restored to a clean level from the northeast (Fig. 3b,



180 v). Pollution in the northwest was earliest removed in Case-3, with Beijing acting like a
181 loophole/passageway in the cleaning process (Fig. 3c, v). These cases presented various pollution
182 distributions, however, all of them were characterized by clear edges or distinct heavy pollution cores.

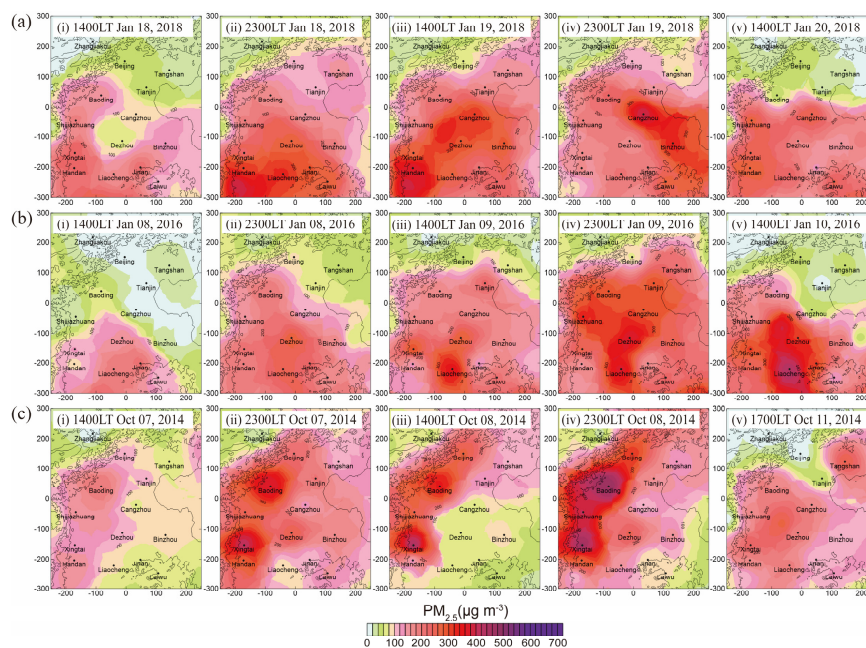


183
184 Figure 2. Temporal evolution of $PM_{2.5}$ concentrations during Case1–3, respectively represent (a) west-
185 southwest wind shear type pollution (January 18–21, 2018), (b) south-north wind shear type pollution
186 (January 7–11, 2016) and (c) topographic obstruction type pollution (October 7–12, 2014). The locations
187 of these $PM_{2.5}$ stations are marked in Fig. 1a.

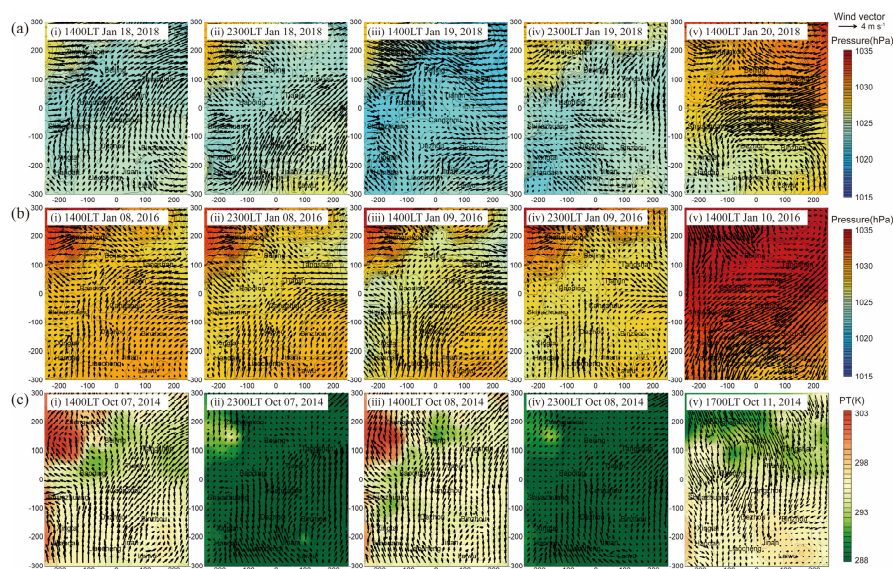
188 The correspondent surface meteorological fields of the three cases are shown in Fig. 4. Case-1 and
189 Case-2 represent the two main modes of the wind shear category which are affected by the dynamic AIBs,
190 and thus the observed sea level pressure and wind fields are discussed (Fig. 4a-b). Case-3 belongs to the
191 topographic obstruction category affected by the AIB created by the cold-air damming, and its potential
192 temperature and wind fields are displayed to focus on the combined action of the thermal and dynamic
193 properties (Fig. 4c). As shown in Fig. 4a, i-iii, the pollution formation and maintenance processes of
194 Case-1 were dominated by a leeward trough, which induced the westerly airflow shear to the southwest
195 wind and produced a convergence belt at the trough axis. As the trough broadened and moved eastward,
196 the wind convergence zone also moved (Fig. 4a, i-iii). On the evening of January 19, 2018, the leeward
197 trough temporarily evolved into an inverted trough under the force of the approaching high-pressure,



198 creating a cyclonic convergence (Fig. 4a, iv). This explains why the heavily polluted center transferred
199 to the east in this episode (refer to Fig. 3a, i-iv). Until January 20, 2018, a high-pressure system invaded
200 the NCP from the northeast, bringing strong northeast winds (Fig. 4a, v), which made the pollution spread
201 southward in turn (refer to Fig. 3a, v). During Case-2, a saddle pressure field persisted in the pollution
202 formation-maintenance stage and induced the prevailing northerly winds in the northern NCP to
203 antagonize the dominant southerly flows in the southern area (Fig. 4b, i-iv). As a result, the polluted air
204 mass was prevented from advancing northward to the mountains, causing a strong contrast between the
205 pollution levels in the northern and southern of the domain (refer to Fig. 3b i-iv). Its pollution diffusion
206 process was also associated with a northeast high-pressure invasion, by strong northeasterly airflows
207 cleaning up the $PM_{2.5}$ (Fig. 4b, v). As for the Case-3 under the topographic obstruction category, there
208 was a narrow area with low potential temperature and weak wind speed at the foot of the mountains on
209 the windward side in the daytime but this feature became fuzzy at night (Fig. 4c, i-iv). This diurnal
210 variation repeatedly occurred during the formation and maintenance stage, which may be an important
211 reason for the day-night difference in pollution distribution (refer to Fig. 3c i-iv). In the end, the strong
212 flows and cold air bursting like a jet stream through a pathway across Zhangjiakou-Beijing-Tianjin (Fig.
213 4c, v), made pollutants begin to be swept out from the northwest (refer to Fig. 3c, v).



214
215 Figure 3. Spatial distributions of surface $PM_{2.5}$ concentrations (shaded colors) at the pollution stages of
216 (i) formation, (ii-iv) maintenance and (v) diffusion during representative Case1-3 under (a) west-
217 southwest wind shear type, (b) south-north wind shear type and (c) topographic obstruction type. Values
218 shown in x- and y-axis denote the distances (km) to the domain center.



219
220 Figure 4. Observed sea level pressure/potential temperature and wind vectors at the pollution stages of
221 (i) formation, (ii-iv) maintenance and (v) diffusion during representative Case1–3 under (a) west-
222 southwest wind shear type, (b) south-north wind shear type and (c) topographic obstruction type. The
223 shaded colors represent the sea level pressure in (a-b) and the potential temperature in (c). The arrows
224 indicate wind vectors. Values shown in x- and y-axis denote the distances (km) to the domain center.

225 3.2 Evaluation of simulated meteorological field

226 To reveal the PBL three-dimensional structure of these representative cases, numerical simulations
227 were conducted using the WRF model. It is necessary to evaluate the model reliability before analyzing
228 the simulated results. The model-observation comparisons in the previous studies usually focus on the
229 time series of surface meteorological elements, such as 10 m wind speed and direction, 2 m temperature
230 and humidity (Rogers et al., 2013; Bei et al., 2018; Qu et al., 2021). The model performance of their
231 spatial fields is often ignored, and the evaluation of the PBL vertical structure is relatively lacking, but
232 the regional distribution and vertical profile of wind-temperature-humidity are crucial for air pollution.
233 In this study, the evaluation was carried out including three perspectives: i) the temporal evolution and
234 ii) the spatial pattern of near-surface potential temperature and wind speed, as well as iii) the vertical
235 profile-temporal structure of these two variables.

236 For the temporal evolution of the near-surface potential temperature and wind speed, the hourly
237 observations and simulations of 13 key cities (Beijing, Tianjin, Shijiazhuang, Baoding, Handan,
238 Tangshan, Cangzhou, Dezhou, Jinan, Weifang, Binzhou, Chengde and Zhangjiakou) evenly distributed
239 in the NCP were compared during these three pollution cases. The model outputs were extracted from
240 the grid points nearest to observed sites. As shown in Table 1, the correlation coefficients of the simulated



241 and observed potential temperature and wind speed were 0.80–0.91 and 0.54–0.64 ($p < 0.01$), respectively.
 242 The statistical results demonstrated that the major variations in the time series of the surface observations
 243 were reproduced by the model, which has also been recognized in previous studies (Rogers et al., 2013;
 244 Bei et al., 2018; Qu et al., 2021).

245 Table 1. Statistics of model performance for near-surface potential temperature and 10 m wind speed for
 246 selected 13 cities during the representative cases.

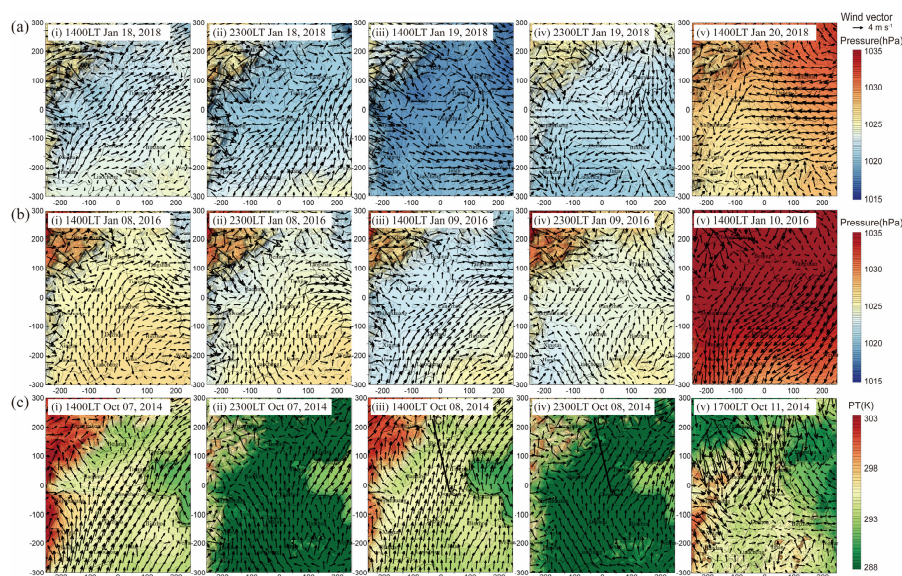
	Case-1				Case-2				Case-3			
	PT		WS		PT		WS		PT		WS	
	R	RMSE	R	RMSE	R	RMSE	R	RMSE	R	RMSE	R	RMSE
Beijing	0.80	2.20	0.62	1.15	0.87	2.60	0.61	1.69	0.91	2.20	0.73	1.65
Tianjin	0.89	2.40	0.66	1.48	0.85	1.90	0.63	1.97	0.92	2.10	0.61	2.13
Shijiazhuang	0.77	2.80	0.52	2.02	0.82	2.50	0.66	1.69	0.88	2.20	0.58	1.95
Baoding	0.83	2.50	0.60	1.34	0.85	2.40	0.61	1.53	0.89	2.30	0.60	1.97
Handan	0.93	1.40	0.48	1.36	0.78	3.20	0.56	2.27	0.95	1.30	0.66	1.94
Tangshan	0.69	4.00	0.62	1.44	0.81	3.30	0.53	1.64	0.85	3.00	0.46	2.24
Cangzhou	0.85	3.00	0.64	1.23	0.79	2.50	0.60	1.92	0.94	2.10	0.75	1.45
Dezhou	0.78	3.70	0.51	1.69	0.87	1.50	0.63	2.82	0.90	2.30	0.55	2.97
Jinan	0.76	2.80	0.49	2.96	0.74	2.40	0.63	2.45	0.91	2.10	0.56	3.10
Weifang	0.79	2.10	0.53	1.42	0.78	2.50	0.71	1.99	0.94	2.10	0.85	1.40
Binzhou	0.81	2.50	0.51	1.97	0.83	2.30	0.86	1.29	0.92	2.00	0.81	1.47
Chengde	0.75	5.10	0.47	2.06	0.63	6.50	0.47	2.60	0.84	3.70	0.56	1.74
Zhangjiakou	0.90	5.40	0.33	2.23	0.77	5.30	0.47	3.13	0.96	4.80	0.54	2.50
Average	0.81	3.07	0.54	1.72	0.80	2.99	0.61	2.08	0.91	2.47	0.64	2.04

247 Case-1: west-southwest wind shear type (January 18–21, 2018); Case-2: south-north wind shear type
 248 (January 7–11, 2016); Case3: topographic obstruction type (October 7–12, 2014). All statistics are
 249 calculated from hourly values.

250 Referring to Fig. 4, the spatial distribution of the simulated sea level pressure/potential temperature
 251 and wind vector during the three cases are displayed in Fig. 5. In Case-1 and Case-2, the leeward trough
 252 and saddle pressure field, as well as the corresponding west-southwest wind shear and south-north wind
 253 shear were reproduced in the simulated fields (Fig. 5a-b, i-iv vs Fig. 4a-b, i-iv). Also, their movement
 254 and evolution during the pollution formation-maintenance processes were also captured by the WRF
 255 model, although there were some small deviations in the specific positions. At the diffusion stage, the
 256 simulated northeastern high-pressure invasion and the prevailing easterly/northeasterly winds were
 257 comparable with the observed fields (Fig. 5a-b, v vs Fig. 4a-b, v). As for Case-3, the surface
 258 meteorological fields output by the model successfully reflected the narrow cold zone and quiet wind
 259 belt at the foot of the mountains, as well as their diurnal variation and sustainability in the pollution
 260 formation-maintenance stage (Fig. 5c, i-iv vs Fig. 4c, i-iv). Even though the area was shorter at its south
 261 end on the afternoon of October 08, 2014, and there was an overestimate of the potential temperature in



262 the northwest mountains and the Bohai Sea at night. At the end of this episode, a strong northerly cold
263 airflow similar to the observation appeared in the simulation field (Fig. 5c, v vs Fig. 4c, v). Generally,
264 the main features of the surface distributions of meteorological observations during these three cases can
265 be reflected well in the simulated fields.

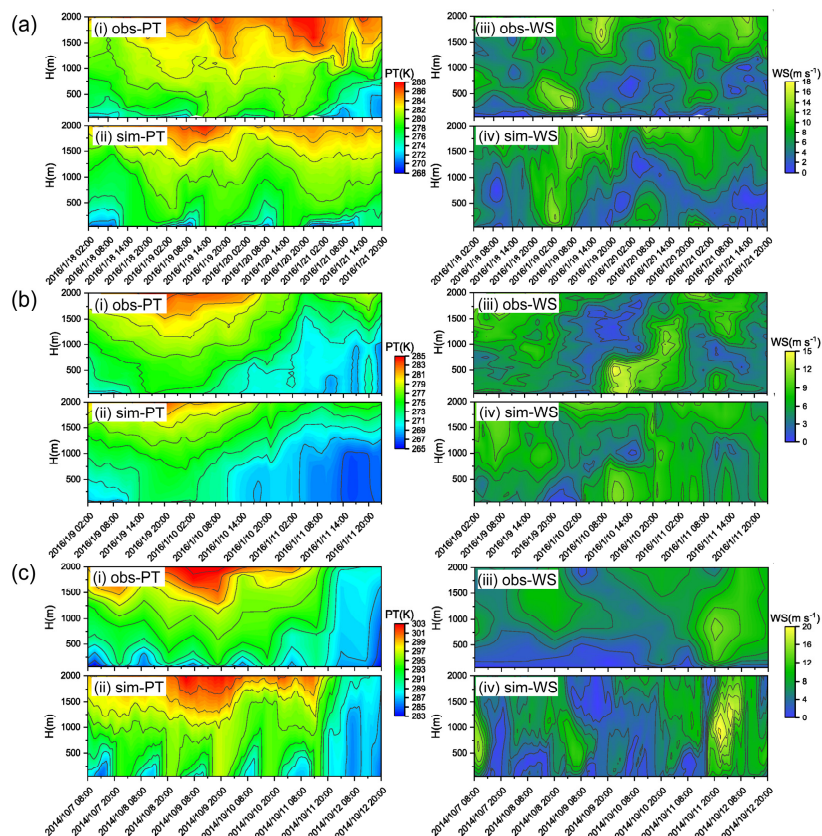


266
267 Figure 5. Simulated sea level pressure/potential temperature and wind vectors at the pollution stages of
268 (i) formation, (ii-iv) maintenance and (v) diffusion during representative Case1-3 under (a) west-
269 southwest wind shear type, (b) south-north wind shear type and (c) topographic obstruction type. The
270 shaded colors represent the sea level pressure in (a-b) and the potential temperature in (c). The arrows
271 indicate wind vectors. Values shown in x- and y-axis denote the distances (km) to the domain center.
272 Lines C_1C_1' in (c) refer to the cross-sections of the potential temperature in Fig. 11.

273 Moreover, the simulated and observed time-height cross sections of potential temperature and wind
274 speed were compared to reveal the model's ability to capture the PBL vertical structure of each case (Fig.
275 6). The observation data of Case-1 and Case-2 were obtained from intensive sounding experiments at the
276 Dezhou site and Cangzhou site, respectively. The observation information during Case-3 was provided
277 by routine soundings at the Beijing site. As for Case-1, the model successfully reproduced thermal
278 structure evolution in the pollution formation-maintenance period, while the final uplift of the inversion
279 layer and the growth of PBL were not captured (Fig. 6a, i-ii). By comparison, the dynamic structures,
280 being the dominant role of this type, were better simulated. The vertical location and temporal transition
281 of the strong and weak wind layers were comparable with observations (Fig. 6a, iii-iv). The model
282 performance during Case-2 was satisfactory both for cross-sections of the potential temperature and wind
283 speed. The formation and decay of upper temperature inversion and the development of the cold



284 convective PBL were consistent between observation and simulation, though there were some
 285 underestimations in the modeled results (Fig. 6b, i-ii). The weak wind layer presented in the maintenance
 286 stage and vertical wind shear that occurred in the diffusion stage were also captured by the model with
 287 smaller gradients (Fig. 6b, iii-iv). In Case-3, the WRF reproduced the observed diurnal cycle of the
 288 potential temperature in the low-level and the continuous warming at the upper layer during the
 289 formation-maintenance process, as well as the replacement of a well-mixed cold air mass in the last phase
 290 (Fig. 6c, i-ii). The evolution of the simulated wind speed was roughly similar to the observation,
 291 including the maintenance of the calm wind layer in the first four days and the appearance of the final
 292 strong wind layer (Fig. 6c, iii-iv). There were some inconsistencies in the details of observation and
 293 simulation evolution, which may result from the coarse resolution of routine soundings in time and
 294 vertical direction, in addition to the uncertainties of model simulation.



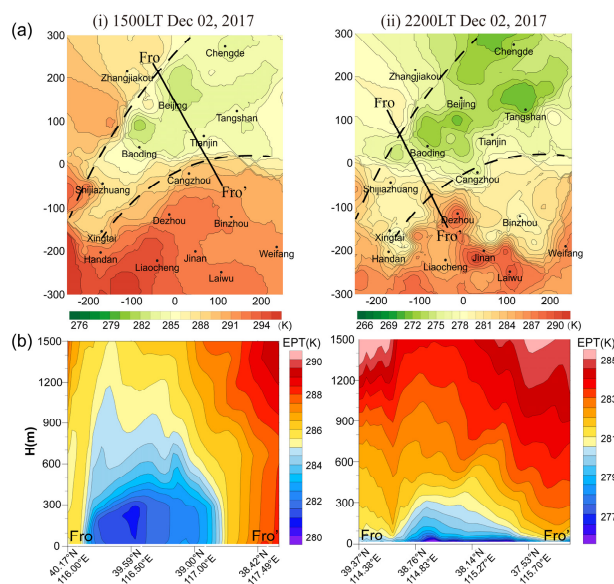
295
 296 Figure 6. Observed and simulated time-height cross sections of potential temperature (left) and wind
 297 speed (right) during representative Case 1–3 under (a) west-southwest wind shear type (January 18–21,
 298 2018), (b) south-north wind shear type (January 9–11, 2016) and (c) topographic obstruction type
 299 (October 7–12, 2014).



300 Overall, the model shows the ability to capture the observed mesoscale systems and atmospheric
301 thermal-dynamic structures reasonably both at the surface and in the vertical direction. With confidence
302 in the model results, we now proceed to a detailed investigation of the PBL spatial structure affected by
303 mesoscale AIBs under various pollution types.

304 3.3 PBL spatial structure under each pollution type

305 We analyze the simulated vertical cross-sections of the mesoscale systems and AIBs to reveal the
306 three-dimensional structure of the PBL. Two key parameters, potential temperature and wind divergence,
307 are used to respectively indicate the thermal stability and dynamic convergence of the PBL, which affect
308 the vertical mixing and horizontal diffusion of $PM_{2.5}$, and are critical to the pollution formation and
309 distribution. Therefore, for the pollution case under the thermally dominated frontal category, dynamical-
310 driven wind shear category, and the thermodynamic-mixture topographic obstruction category, the
311 potential temperature section, wind divergence section and both of them are respectively displayed and
312 discussed.



313
314 Figure 7. Re-display of Figs. 5&7 in Jin et al. (2021). (a) Surface distributions and (b) vertical cross-
315 sections of equivalent potential temperature at (i) 1500 LT and (ii) 2200 LT on December 2, 2017, in
316 frontal category case. Dashed and solid lines in (a) respectively indicate the locations of the AIBs and
317 the sections.

318 Frontal category

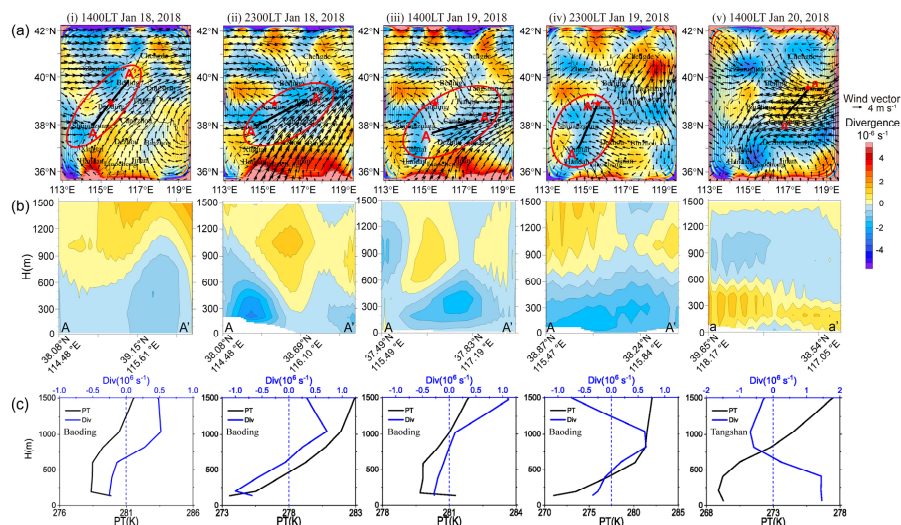
319 The three-dimensional thermal structure of the PBL under the frontal category has been revealed in



320 a previous case study (Jin et al., 2021). Statistics show that this kind of mesoscale PBL structure occurs
 321 most frequently and tends to result in the most severe pollution levels in the NCP, so we recapitulate it
 322 again here. As shown in Fig.7 (the re-display of Figs. 5&8 in Jin et al. (2021)), the boundary layer was
 323 characterized by an isolated cold air mass, which was laterally confined by mountains and warm front
 324 AIB (Fig.7a-b), and vertically covered by a warm dome (Fig.7c-d). The elevated inversion strength was
 325 as high as 3~6 K 100 m⁻¹, making the PBL height drop abruptly to 200~300 m in the cold area from
 326 600~800 m outside the zone (Fig.7c). The contrast of the PBL thermal structure was unobvious during
 327 nighttime, with surface inversion over the whole region (Fig.7d). However, the nocturnal inversion layer
 328 was thicker and stronger in the cold area, making the PBL height lower than in the warmer area. The
 329 shallow stable stratified PBL structure persisted throughout the daytime and night, which constituted
 330 adverse dispersion conditions and further resulted in the most serious PM_{2.5} pollution.

331 Wind shear category

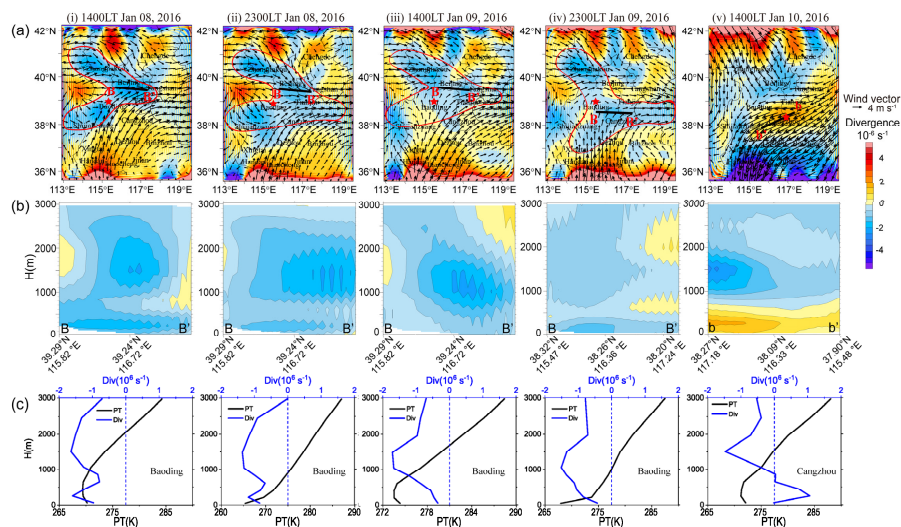
332 This pollution category, consisting of three subtypes of west-southwest wind shear, southeast-east
 333 wind shear and south-north wind shear, is mainly driven by dynamic flows. Therefore, the wind
 334 divergence features, including near-surface horizontal distributions, vertical cross-sections and vertical
 335 profiles are considered. Among these subtypes, the dynamic characteristics of the first two are similar,
 336 so we only analyze the representative cases of the first and the third subtypes, in the following.



337 Figure 8. (a) Surface spatial distributions, (b) vertical cross-sections and (c) vertical profiles of the
 338 simulated wind divergence at the pollution stages of (i) formation, (ii-iv) maintenance and (v) diffusion
 339 during representative Case-1 under west-southwest wind shear type. The red ellipses, black lines and red
 340 pentacles in (a) indicate the convergence belt, the section lines in (b) and the profile sites in (c),
 341 respectively. The potential temperature profiles are presented in (c) to indicate the boundary layer top.
 342



343 Figure 8 displays the PBL dynamic structure of Case-1 which belongs to the west-southwest wind
 344 shear type. During the pollution formation-maintenance stage, westerly winds shifted to southwesterly
 345 winds at the trough axis and thus formed a convergence belt at the surface with a divergence of
 346 $-2\sim-4\times 10^{-6} \text{ s}^{-1}$. This trough-convergence belt continued to move to the southeast, and evolved into a
 347 cyclonic-convergence center at the end of the maintenance phase (Fig. 8a, i-iv). The vertical sections of
 348 the surface convergence belt show that the depth of the convergence layers did not exceed 1000 m, with
 349 compensating divergence layer immediately above it (Fig. 8b, i-iv). Furthermore, the vertical profiles of
 350 the wind divergence and potential temperature at the Baoding site located in the convergence belt were
 351 extracted to illustrate PBL dynamic structure more clearly. It can be found that the mutation of divergence
 352 value and the jump of potential temperature roughly appeared at the same height (Fig. 8c, i-iv), which
 353 demonstrated the vertical scale of the wind convergence belt was equivalent to the depth of the PBL.
 354 This phenomenon reveals that the west-southwest wind convergence caused by the trough mainly occurs
 355 within the PBL, reflecting its mesoscale property. In the process of pollution diffusion, divergent wind
 356 fields first occurred in the northeastern area (Fig. 8a, v). The vertical cross-section of this divergent layer
 357 and vertical profiles at the Tangshan site show that the northeast wind divergence layer was relatively
 358 thin with a thickness of no more than 600 m (Fig. 8b-c, v), meaning that the removal of pollutants only
 359 occurred in the low-level atmosphere.



360 Figure 9. Same as Fig. 8, but for representative Case-2 under south-north wind shear type. The red lying-
 361 Y shapes, black lines and red pentacles in (a) indicate the convergence belt, the section lines in (b) and
 362 the profile sites in (c), respectively.

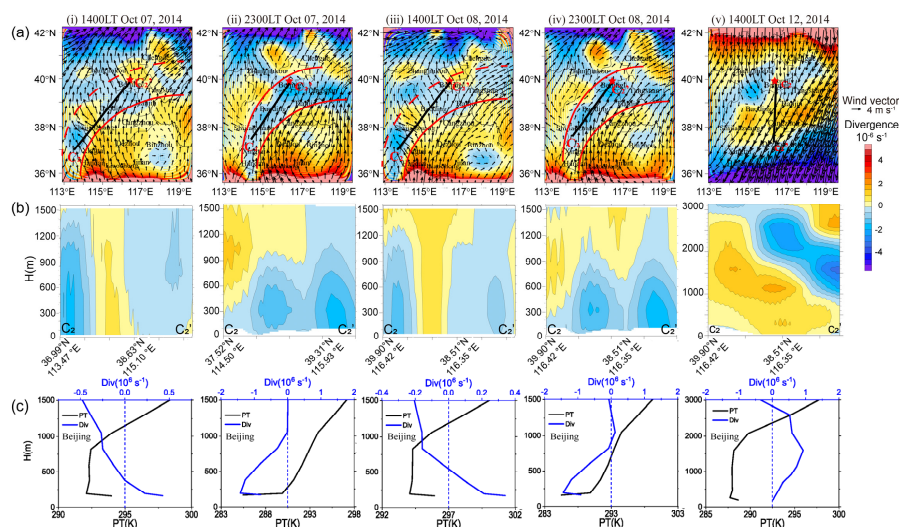
364 As for the south-north wind shear type, the surface divergence fields displayed a "lying Y shaped"
 365 convergence zone with the opening to the left during the pollution formation-maintenance stage of the



366 representative Case-2 (Fig. 9a, i-iv), which was caused by the meeting of the southerly winds and the
367 northerly winds and then turning to the easterly winds. The vertical cross-sections of this special
368 convergence zone exhibited a depth extending upwards for more than 3000 m, with a peak between 1000
369 m and 2000 m (Fig. 9b, i-iv). With reference to the vertical profiles of wind divergence and potential
370 temperature at the Baoding site, it can be seen that the depth of the convergence layer under this shear
371 type far exceeded the height of the PBL, whether it was in the daytime or the night (Fig. 9c, i-iv). These
372 phenomena prove that the south-north wind shear created by the saddle pressure field was exceeded the
373 scale of a typical mesoscale meteorological process. The vertical scale of the dynamic feature was no
374 longer limited to the PBL, implying the sub-synoptic scale characteristics. In the pollution diffusion stage
375 of this case, the PBL structure was the same as in Case-1 (Fig. 9a-c, v), and has been described in the last
376 paragraph.

377 Topographic obstruction category

378 As an outcome of a mixture of thermal and dynamic effects, the topographic obstruction category
379 pollution is analyzed from the perspectives of both the wind divergence and potential temperature to
380 reveal the thermal and dynamic structure of the PBL.



381

382 Figure 10. Same as Fig. 8, but for representative Case-3 under topographic obstruction type. The red
383 curves, black lines and red pentacles in (a) indicate the convergence belt, the section lines in (b) and the
384 profile sites in (c), respectively.

385 Figure 10 shows the dynamic characteristics of the PBL during the representative Case-3. In the
386 pollution formation-maintenance stage, there was an arc-shaped convergence belt at the foot of the
387 mountains on the windward, due to the momentum loss in the northward flow under the action of
388 topographic obstruction (Fig. 10a, i-iv). The shape of this convergent belt was more regular at night (Fig.

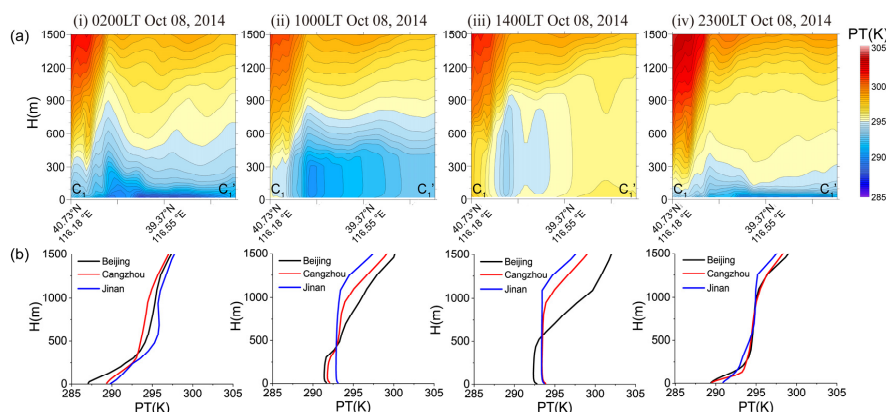


389 10a, ii, iv) but had some breakages at the northwest edge during the day when there was a local southeast
390 wind around Beijing and Shijiazhuang (Fig. 10a, i, iii). The vertical sections also reflected the general
391 features and diurnal difference, manifested as an integral convergence layer with the depth approximating
392 the height of the mountain at night (Fig. 10b, ii, iv), and an isolated divergent layer emerged during the
393 daytime (Fig. 10b, i, iii). The vertical profiles of the wind divergence and potential temperature at Beijing
394 were further extracted shown in Fig. 10c, i-iv. In the evening, the atmosphere below 1200 m was
395 convergent with the peak appearing near the surface about $-1.5 \times 10^{-6} \text{ s}^{-1}$. In the afternoon, there was a
396 weak divergence layer with a strength of about $0.5 \times 10^{-6} \text{ s}^{-1}$ and a thickness of about 200~300 m within
397 the PBL. We infer that the day-night variation may be the consequence of the mountain-valley circulation,
398 where northwestward daytime valley winds developed along the mountain passes near Beijing and
399 Shijiazhuang leading to flow divergence, and downslope winds formed at night strengthening the surface
400 wind convergence. When the pollution began to spread, the northern part of the domain was in a strong
401 divergence condition (Fig. 10a, v). The corresponding cross-section shows that the north wind divergence
402 layer was very deep (nearly 3000 m), gradually thinning from north to south (Fig. 10b, v). Moreover, the
403 vertical profiles of the divergence and potential temperature at the Beijing site prove that the PBL was
404 well developed up to 2000 m, accompanied by strong horizontal divergence throughout the layer (Fig.
405 10c, v), both of which indicate extremely favorable ventilation conditions.

406 The thermal properties and their evolution, especially diurnal variation, play an important role in
407 this type of pollution pattern, which has been presented in the previous surface analysis. Hence, we
408 further explore the three-dimension thermal structure of the PBL, taking the vertical cross-sections of
409 potential temperature across the characteristic cold area in the pollution maintenance stage (October 8,
410 2014, the location of cross-section shown in Fig. 5c) as an illustration. In the early hours of the morning,
411 although there were surface inversions, the cold air masses in front of the mountains were much thicker
412 (Fig. 11a, i). After sunrise, the convective boundary layer developed both in the front of the mountains
413 and in the plain due to the surface heating, but the temperature in the southern plain was higher (Fig. 11a,
414 ii). In the afternoon, a deep, well-mixed warm PBL has formed in the southern plains while a cold air
415 mass capped by strong inversion still remained in the northern piedmont area (Fig. 11a, iii). At night,
416 large amounts of cold air accumulated at the foot of the mountains again (Fig. 11a, iv). The vertical
417 profiles of the simulated potential temperature of the three cities from south to north, Jinan, Cangzhou
418 and Beijing, also support this thermal evolution process. At 0200 LT, there were surface inversions at all
419 three cities, and Beijing had the strongest inversion intensity of about $2 \text{ K } 100 \text{ m}^{-1}$ (Fig. 11b, i). By 1000
420 LT, the PBL in Jinan had increased to 1100 m, while the convective boundary layers in Beijing and
421 Cangzhou were shallow (about 400 m, Fig. 11b, ii). In the afternoon, the PBL was fully developed with
422 the height from the south to the north site ranging from 1150 m to 650 m, and there was still a thick
423 inversion layer above Beijing (Fig. 11b, iii). At 2300 LT, the surface inversion at the three sites has



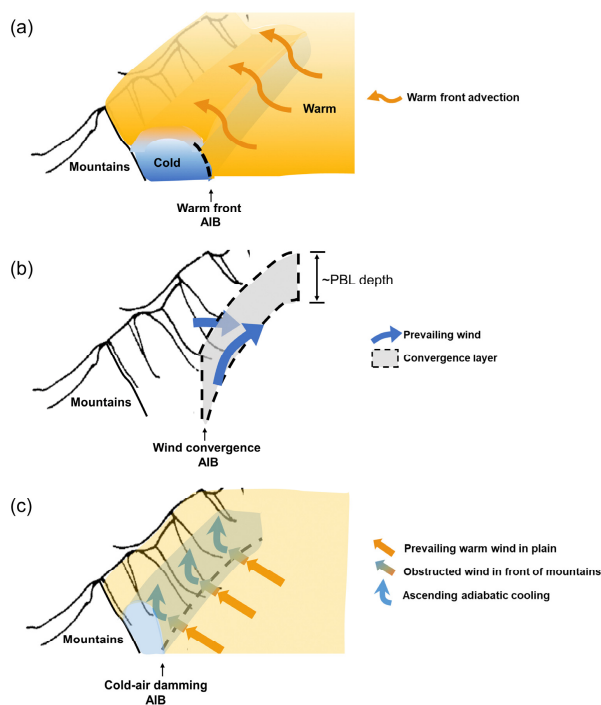
424 formed again (Fig. 11b, iv). The persistent cold air mass in front of the mountains is similar to the cold-
425 air damming on the eastern side of Appalachian (Bell and Bosart, 1988). The prevailing southerly warm
426 airflows were blocked by the mountains and the geostrophic balance was disrupted so that the heat cannot
427 reach the foothills and the air further accumulated and ascended here for adiabatic cooling. It should be
428 noted that the southeast edge of this cold area was more pronounced during the daytime (Fig. 4c, Fig.
429 11), in comparison to that at the night. This is reasonable given that the nocturnal boundary layer was
430 stable over the whole domain and more susceptible to the local property. Although the AIB was relatively
431 unclear at the surface during nighttime, the nocturnal cold layer at the foothills was deeper than the
432 southern plain area, probably due to the cold drainage flows along the sidewall of the mountains forming
433 a cold air pool. This diurnal cycle of the PBL thermal structure can well explain the day-night difference
434 in pollution distribution pattern (Fig. 3e). Shortly speaking, the PBL thermal structure during the
435 formation-maintenance stage under the topographic obstruction category pollution is a manifestation of
436 cold-air damming AIB, assisted by the role of cold air pool at night (Fig. 4c).



437
438 Figure 11. (a) Vertical cross-sections and (b) vertical profiles of the simulated potential temperature at
439 (i) 0200 LT, (ii) 1000 LT, (iii) 1400 LT and (iv) 2300 LT on October 08, 2014 in Case-3 under the
440 topographic obstruction type. The cross-sections C_1C_1' are shown Fig. 5c, iii, iv.

441 4 Summary and discussion

442 The three-dimensional PBL structures modified by the mesoscale systems and interacted with the
443 AIBs under various pollution types in the NCP, as well as the ability of the mesoscale meteorological
444 model (WRF) in simulating these processes, were investigated in this study. The pollution types were
445 classified from pollution episodes during autumn and winter of 7 years (2014–2020) in Jin et al. (2022
446 submitted). Representative cases under these types were simulated by the WRF model in this study. The
447 model was comprehensively evaluated for its reliability, by comparison with observed PBL vertical
448 structure, as well as the temporal series and spatial evolution of the surface meteorological fields.



449

450 Figure 12. Schematic diagram showing the conceptual model of PBL spatial structures under three
451 categories pollution. (a) Frontal category: the blue-shaded and orange-filled areas represent the isolated
452 and stable cold air mass in front of the front and the warm well-mixing atmosphere behind the front. The
453 orange arrows represent warm front advection. (b) Wind shear category: two blue arrows represent the
454 airflows ahead of and behind the trough. The gray-filled area indicates the dynamic convergence layer
455 equal in height to the boundary layer. (c) Topographic obstruction category: the light blue filled area
456 indicates the cold-air damming at the foot of the windward mountains. It is the result of the regional
457 warm airflows (long orange arrows) being blocked by topography (short gradient-color arrows) and then
458 accumulating to ascend cooling (up blue arrows). Black dashed lines in (a-c) indicate the warm front
459 AIB, wind convergence AIB, and cold-air damming AIB, respectively.

460 Based on results of this paper, more complete and clearer view of the PBL spatial structures during
461 pollution episodes in the regional scale of NCP can be obtained, as schematically shown in Fig.12. All
462 the pollution conditions were classified into three categories. The most prominent was the frontal
463 category. With an isolated cold air mass laterally bounded by the warm frontal AIB in one side and
464 mountains in another side, the PBL was vertically suppressed by a dome-like warm cap. Typically, the
465 intensity of the frontal inversion can be as large as $3\sim 6\text{ K }100\text{ m}^{-1}$. As a consequence, the PBL in this
466 cold area was very shallow (as low as $200\sim 300\text{ m}$) and kept stable stratification, in sharp contrast to the



467 deep and well-mixing boundary layer outside this zone (Fig. 12a). This explained why $PM_{2.5}$ accumulated
468 rapidly in this enclosed and stable space and formed a laterally clearly defined polluted air mass.
469 Diurnally, the nocturnal PBL in this category was less typical as its daytime counterpart. The thermal
470 structure of the PBL played a leading role in this category, resulting in the most severe pollution level.

471 The second category was dominated by dynamic processes. Three modes compounded this category,
472 i.e., west-southwest wind shear type, southeast-east wind shear type and south-north wind shear type.
473 The first two types were characterized by the leeward trough (or inverted trough). A convergence layer
474 lay in the wind shear zone with the thickness of the PBL depth (Fig. 12b), with a typical near-surface
475 divergence of $-2\sim-4\times 10^{-6} s^{-1}$, and accompanied by a compensating divergence layer above the PBL,
476 which reflected the mesoscale property of the trough AIB. The third type displayed a "lying Y shaped"
477 convergence layer from the surface extending upwards to about 3000 m, with a convergence peak above
478 the PBL top (not shown in Fig. 12). This implied the sub-synoptic scale features. In this category, the
479 boundary layer was dominated by dynamic convergence effects, which made pollutants accumulate, and
480 the pollution level in the NCP was relatively light.

481 The topographic obstruction pollution category was characterized by a cold-air damming AIB at the
482 foot of the windward side of the mountains. It usually occurred when the southerly winds were too weak
483 to cross the terrain barrier and the northward flows were blocked, which allowed air masses to accumulate
484 and ascend cooling in front of the mountains. The PBL air was cold and capped by a strong inversion in
485 the damming area, in contrast with well-mixed warm PBL in the southern plains. Meanwhile, the air
486 flows were convergent in front of the mountains. These general characterizes are shown in Fig. 12c. In
487 more detail, the thermal discontinuity became indistinct at night due to the surface inversion over the
488 whole domain, while the nocturnal wind convergence belt was more pronounced. The diurnal variation
489 of the PBL dynamic and thermal structure made the pollutants concentrate at the foot of the mountains
490 during the daytime and distribute throughout the entire plain at night.

491 It should be emphasized that the above results are highly dependent on numerical simulation, due
492 to the scarcity and limitation of PBL sounding data. Evaluation from the spatial-temporal variation of the
493 surface meteorological field and PBL vertical structure indicates that the model performance was good.
494 WRF can capture mesoscale systems and AIBs, as well as their overall evolution process and diurnal
495 variation. However, it was still difficult to reproduce the precise timing of the buildup and breakup as
496 well the exact location and range of these systems. This deficiency should be concerned seriously when
497 simulated meteorological fields are used to drive air quality models, since a small position bias and time
498 deviation of the AIBs can significantly alter pollution levels at a certain site (Seaman, 2000; McNider
499 and Pour-Biazar, 2020). In the present study, we focus on the major characteristics of the PBL spatial
500 structure, which were reasonably reflected in the model results.

501 In addition to the inevitable uncertainty of the numerical simulation, the classification proposed in



502 this paper might still be roughly or oversimplified. Real processes may be more complex and atypical as
503 analyzed in this paper. However, this work, to the authors' knowledge, is the first trial to classify the PBL
504 structure over the vast scale of the NCP, and to clarify its role on regional PM_{2.5} pollution. Modulation
505 of the PBL by mesoscale meteorological processes, particularly the AIBs, is emphasized. Extending the
506 view of the PBL from local vertical properties to mesoscale three-dimension structures may be a step
507 toward a better understanding of the meteorological effects on regional-scale PM_{2.5} pollution.

508 **Data availability**

509 The data in this study are available from the corresponding author (xhcai@pku.edu.cn).

510 **Author contribution**

511 XHC and XPJ designed the research. MYY and HSZ collected the data. XPJ performed the simulations
512 and wrote the paper. XHC reviewed and commented on the paper. YS, XSW and TZ participated in the
513 discussion of the article.

514 **Competing interests**

515 The authors declare that they have no conflict of interest.

516 **Acknowledgements**

517 This work was supported by National Key Research and Development Program of China
518 (2018YFC0213204).

519 **References**

- 520 Baumann, K., Maurer, H., Rau, G., Piringer, M., Pechinger, U., Prevot, A., Furger, M., Neining, B. and
521 Pellegrini, U.: The influence of south Foehn on the ozone distribution in the Alpine Rhine valley -
522 results from the MAP field phase, *Atmos. Environ.*, 35(36), 6379-6390, doi:10.1016/s1352-
523 2310(01)00364-8, 2001.
- 524 Bei, N. F., Zhao, L. N. Wu, J. R., Li, X., Feng, T. and Li, G. H.: Impacts of sea-land and mountain-valley
525 circulations on the air pollution in Beijing-Tianjin-Hebei (BTH): A case study, *Environ. Pollut.*, 234,
526 429-438, doi:10.1016/j.envpol.2017.11.066, 2018.
- 527 Bell, G. D. and Bosart, L. F.: Appalachian cold-air damming. *Mon. Wea. Rev.*, 116, 137-161,



- 528 doi:10.1175/1520-0493(1988)116,0137:ACAD.2.0.CO;2, 1988.
- 529 Berger, B. W. and Friehe, C. A.: Boundary-layer structure near the cold-front of a marine cyclone during
530 “ERICA”, *Bound.-Layer Meteor.*, 317-317, doi:10.1007/BF0071125874, 1995.
- 531 Bianco, L., Djalalova, I. V., King, C. W., and Wilczak, J. M.: Diurnal Evolution and Annual Variability
532 of Boundary-Layer Height and Its Correlation to Other Meteorological Variables in California's
533 Central Valley, *Bound.-Layer Meteor.*, 140, 491-511, doi:10.1007/s10546-011-9622-4, 2011.
- 534 Boutle, I. A., Beare, R. J., Belcher, S. E., Brown, A. R., and Plant, R. S.: The Moist Boundary Layer
535 under a Mid-latitude Weather System, *Bound.-Layer Meteor.*, 134, 367-386, doi:10.1007/s10546-
536 009-9452-9, 2010.
- 537 De Wekker, S. F. J.: Observational and numerical evidence of depressed convective boundary layer
538 heights near a mountain base, *J. Appl. Meteorol. Climatol.*, 47, 1017-1026,
539 doi:10.1175/2007jamc1651.1, 2008.
- 540 Dupont, J. C., Haefelin, M., Badosa, J., Elias, T., Favez, O., Petit, J. E., Meleux, F., Sciare, J., Crenn, V.,
541 Bonne, J. L.: Role of the boundary layer dynamics effects on an extreme air pollution event in Paris.
542 *Atmos. Environ.*, 141, 571–579, doi:10.1016/j.atmosenv.2016.06.061, 2016.
- 543 Emeis, S., and Schafer, K.: Remote sensing methods to investigate boundary-layer structures relevant to
544 air pollution in cities, *Bound.-Layer Meteor.*, 121, 377-385, doi:10.1007/s10546-006-9068-2, 2006.
- 545 Garratt, J. R: *The Atmospheric Boundary Layer*. Cambridge University Press, Cambridge, 1992.
- 546 Garratt, J. R.: The internal boundary-layer-A review, *Bound.-Layer Meteor.*, 50, 171-203,
547 doi:10.1007/bf00120524, 1990.
- 548 Hanna, S. R. and Yang, R.: Evaluations of mesoscale models' simulations of near-surface winds,
549 temperature gradients, and mixing depths. *J. Appl. Meteorol.* 40 (6):1095–104, doi:10.1175/1520-
550 0450(2001)040<1095:EOMMSO>2.0.CO;2, 2001.
- 551 Jimenez, P. A., de Arellano, J. V. G., Dudhia, J., and Bosveld, F. C.: Role of synoptic- and meso-scales
552 on the evolution of the boundary-layer wind profile over a coastal region: the near-coast diurnal
553 acceleration, *Meteorol. Atmos. Phys.*, 128, 39-56, doi:10.1007/s00703-015-0400-6, 2016.
- 554 Jin, X. P., Cai, X. H., Yu, M. Y., Song, Y., Wang, X. S., Kang, L. and Zhang, H. S.: Diagnostic analysis
555 of wintertime PM_{2.5} pollution in the North China Plain: The impacts of regional transport and
556 atmospheric boundary layer variation. *Atmos. Environ.*, 224, 117346, doi:
557 10.1016/j.atmosenv.2020.117346, 2020.
- 558 Jin, X. P., Cai, X. H., Yu, M. Y., Wang, X. B., , Song, Y., Wang, X. S., Zhang, H. S. and Zhu, T.: Regional
559 PM_{2.5} pollution confined by atmospheric internal boundaries in the North China Plain: 1. Analysis
560 based on surface observations, *Atmos. Chem. Phys.* (submitted), 2022.
- 561 Jin, X. P., Cai, X. H., Yu, M. Y., Wang, X. S., Song, Y., Kang, L., Zhang, H. S. and Zhu, T.: Mesoscale
562 structure of the atmospheric boundary layer and its impact on regional air pollution: A case study,



- 563 Atmos. Environ., 258, doi:10.1016/j.atmosenv.2021.118511, 2021.
- 564 Lareau, N.P., Crosman, E., Whiteman, C. D., Horel, J. D., Hoch, S.W., Brown, W.O.J. and Horst, T.W.:
565 The persistent cold-air pool study, *Bull. Amer. Meteor. Soc.*, 94, 51-63, doi: 10.1175/BAMS-D-11-
566 00255.1, 2013.
- 567 Li, J., Sun, J. L., Zhou, M. Y., Cheng, Z. G., Li, Q. C., Cao, X. Y. and Zhang, J. J.: Observational analyses
568 of dramatic developments of a severe air pollution event in the Beijing area. *Atmos. Chem. Phys.*
569 18, 3919-3935, doi: 10.5194/acp-18-3919-2018, 2018.
- 570 Li, Q. H., Wu, B. G., Liu, J. L., Zhang, H. S., Cai, X. H. and Song, Y.: Characteristics of the atmospheric
571 boundary layer and its relation with PM_{2.5} during haze episodes in winter in the North China Plain.
572 *Atmos. Environ.* 223, 117265, doi:org/10.1016/j.atmosenv.2020.117265, 2020.
- 573 Liu, N., Zhou, S., Liu, C. S., and Guo, J. P.: Synoptic circulation pattern and boundary layer structure
574 associated with PM_{2.5} during wintertime haze pollution episodes in Shanghai, *Atmos. Res.*, 228,
575 186-195, doi:10.1016/j.atmosres.2019.06.001, 2019.
- 576 Liu, S. and Liang, X. Z.: Observed diurnal cycle climatology of planetary boundary layer height, *J.*
577 *Climate*, 23(21), 5790–5809, doi:10.1175/2010jcli3552.1, 2010.
- 578 Lu, R. and Turco, R. P.: Air pollution transport in a coastal environment II: 3-dimension simulations over
579 Los-Angeles basin, *Atmos. Environ.*, 29(13), 1499-1518, doi:10.1016/1352-2310(95)00015-q,
580 1995.
- 581 Mayfield, J. A. and Fochesatto, G. J.: The Layered Structure of the Winter Atmospheric Boundary Layer
582 in the Interior of Alaska, *J. Appl. Meteorol. Climatol.*, 52, 953-973, doi:10.1175/jamc-d-12-01.1,
583 2013.
- 584 McNider, R. T. and Pour-Biazar, A.: Meteorological modeling relevant to mesoscale and regional air
585 quality applications: a review, *J. Air Waste Manage. Assoc.*, 70, 2-43,
586 doi:10.1080/10962247.2019.1694602, 2020.
- 587 Miao, Y. C. and Liu, S. H.: Linkages between aerosol pollution and planetary boundary layer structure
588 in China, *Sci. Total Environ.*, 650, 288-296, doi:10.1016/j.scitotenv.2018.09.032, 2019.
- 589 Miao, Y. C., Hu, X. M., Liu, S. H., Qian, T. T., Xue, M., Zheng, Y. J. and Wang, S.: Seasonal variation of
590 local atmospheric circulations and boundary layer structure in the Beijing-Tianjin-Hebei region and
591 implications for air quality, *J. Adv. Model. Earth Syst.*, 7(4), 1602-1626,
592 doi:10.1002/2015ms000522, 2015.
- 593 Narasimha, R., Sikka, D. R. and Prabhu, A.: The Monsoon Trough Boundary Layer. *Indian Academy of*
594 *Sciences*, 422 pp, 1997.
- 595 Peng, H. Q., Liu, D. Y., Zhou, B., Su, Y., Wu, J. M., Shen, H., Wei, J. S., and Cao, L.: Boundary-Layer
596 Characteristics of Persistent Regional Haze Events and Heavy Haze Days in Eastern China, *Adv.*
597 *Meteorol.*, doi:10.1155/2016/6950154, 2016.



- 598 Petaja, T., Jarvi, L., Kerminen, V. M., Ding, A. J., Sun, J. N., Nie, W., Kujansuu, J., Virkkula, A., Yang,
599 X. Q., Fu, C. B., Zilitinkevich, S. and Kulmala, M.: Enhanced air pollution via aerosol-boundary
600 layer feedback in China. *Sci Rep* 6, 6, doi:10.1038/srep18998, 2016.
- 601 Pielke, R. A. and Uliasz, M.: Use of meteorological models as input to regional and mesoscale air quality
602 models—Limitations and strengths. *Atmos. Environ.*, 32(8):1455–66, doi:10.1016/S1352-
603 2310(97)00140-4, 1998.
- 604 Potty, K. V. J., Mohanty, U. C., and Raman, S.: Simulation of boundary layer structure over the Indian
605 summer monsoon trough during the passage of a depression, *J. Appl. Meteorol.*, 40, 1241-1254,
606 doi:10.1175/1520-0450(2001)040<1241:sobls>2.0.co;2, 2001.
- 607 Prezerakos, N. G.: Lower tropospheric structure and synoptic scale circulation patterns during prolonged
608 temperature inversions over Athens, Greece, *Theor. Appl. Climatol.*, 60, 63-76,
609 doi:10.1007/s007040050034, 1998.
- 610 Qu, K., Wang, X. S., Yan, Y., Shen, J., Xiao, T., Dong, H. B., Zeng, L. M. and Zhang, Y. H.: A comparative
611 study to reveal the influence of typhoons on the transport, production and accumulation of O₃ in
612 the Pearl River Delta, China, *Atmos. Chem. Phys.*, 21, 11593-11612, doi:10.5194/acp-21-11593-
613 2021, 2021.
- 614 Rajkumar, G., Saraswat, R. S., and Chakravarty, B.: Thermodynamic structure of the monsoon boundary-
615 layer under the influence of a large-scale depression, *Bound.-Layer Meteorol.*, 68, 131-137,
616 doi:10.1007/bf00712667, 1994.
- 617 Ren, Y., Zhang, H. S., Wei, W., Wu, B. G., Cai, X. H. and Song, Y.: Effects of turbulence structure and
618 urbanization on the heavy haze pollution process, *Atmos. Chem. Phys.*, 19, 1041-1057,
619 doi:10.5194/acp-19-1041-2019, 2019.
- 620 Rogers, R. E., Deng, A. J., Stauffer, D. R., Gaudet, B. J., Jia, Y. Q., Soong, S. T. and Tanrikulu, S.:
621 Application of the Weather Research and Forecasting Model for Air Quality Modeling in the San
622 Francisco Bay Area, *J. Appl. Meteorol. Climatol.*, 52, 1953-1973, doi:10.1175/jamc-d-12-
623 0280.1, 2013.
- 624 Seaman, N. L. and Michelson, S. A.: Mesoscale meteorological structure of a high-ozone episode during
625 the 1995 NARSTO-Northeast study, *J. Appl. Meteorol.*, 39, 384-398, doi:10.1175/1520-
626 0450(2000)039<0384:mmsoah>2.0.co;2, 2000.
- 627 Seaman, N. L.: Meteorological modeling for air-quality assessments. *Atmos. Environ.* 34 (12–14):2231–
628 59, doi:10.1016/S1352-2310(99)00466-5., 2000.
- 629 Seibert, R.: South foehn studies since the ALPEX experiment, *Meteorol. Atmos. Phys.*, 43, 91–103,
630 doi:10.1007/BF01028112, 1990.
- 631 Sinclair, V. A., Belcher, S. E., and Gray, S. L.: Synoptic Controls on Boundary-Layer Characteristics,
632 *Bound.-Layer Meteorol.*, 134, 387-409, doi:10.1007/s10546-009-9455-6, 2010.



- 633 Sinclair, V. A.: A 6-yr Climatology of Fronts Affecting Helsinki, Finland, and Their Boundary Layer
634 Structure, *J. Appl. Meteorol. Climatol.*, 52, 2106-2124, doi:10.1175/jamc-d-12-0318.1, 2013.
- 635 Stull, R.: *An Introduction to Boundary Layer Meteorology*. Springer, New York, 1988.
- 636 Talbot, C., Augustin, P., Leroy, C., Willart, V., Delbarre, H., and Khomenko, G.: Impact of a sea breeze
637 on the boundary-layer dynamics and the atmospheric stratification in a coastal area of the North Sea,
638 *Bound.-Layer Meteor.*, 125, 133-154, doi:10.1007/s10546-007-9185-6, 2007.
- 639 Tennekes, H.: The atmospheric boundary layer. *Phys. Today* 27, 52–63, doi:10.1063/1.3128397, 1974.
- 640 Xiao, Z. S., Miao, Y. C., Du, X. H., Tang, W., Yu, Y., Zhang, X., and Che, H. Z.: Impacts of regional
641 transport and boundary layer structure on the PM_{2.5} pollution in Wuhan, Central China, *Atmos.*
642 *Environ.*, 230, doi:10.1016/j.atmosenv.2020.117508, 2020.